

A Vortex-Pump Based Optically-Transparent Microfluidic Platform for Biotech and Medical Applications

Kin Fong Lei^{1,2}, Wing Cheung Law³, Yick-Keung Suen⁴, Wen J. Li^{1,2,*} and Yeung Yam², Ho Pui Ho³, and Siu-Kai Kong⁴

¹Centre for Micro and Nano Systems, ²Department of Automation and Computer-Aided Engineering,

³Center for Advanced Research in Photonics, Department of Electronic Engineering,

⁴Department of Biochemistry, Faculty of Science,

The Chinese University of Hong Kong, Shatin, Hong Kong SAR

*Contact Author: wen@acae.cuhk.edu.hk

Abstract – This paper reports an automated polymer based microfluidic analysis system integrated with a surface plasmon resonance (SPR) biosensor that demonstrates the detection of specific binding of biomolecules and that qualitatively monitors cell adhesion on the sensor surface. Micropumps, microchannels, and a SPR biosensor were integrated into a single polymer (PMMA) based microfluidic system. The integrated system has been studied for its potential applications in bio-molecules detection and drugs discovery. Two experiments, 1) monitoring the reaction between the BSA-BSA antibody, and 2) monitoring the activities of living cells in the presence or absence of trypsin in a RPMI-1640 medium, were conducted to show the bio-medical application capability. Because SPR based bio-detection requires optically transparent substrates, PMMA is a potential replacement for glass and silicon-glass in microfluidic systems, if bio-compatibility and low-cost are desired. Hence, our work has shown the feasibility of commercializing a SPR based bio-medical/chemical analyses system in the near future.

Keywords – *microfluidic systems; SPR biosensor; bio-medical microfluidics.*

I. INTRODUCTION

In the past decade, microfluidic devices have emerged as a challenging area of research in micro-electro-mechanical systems (MEMS). Various microfluidic devices have been developed including a microvalve [1], micropump [2], micromixer [3], microchannel network [4], and a microfluidic flow sensor [5]. A microfluidic system, which consists of several microfluidic devices, is designed to sense, regenerate, and deliver fluid volumes on the order of micro-liters. The large-scale integration of microfluidic devices is a trend in the advancement of microfluidic technology [6].

Microfluidic systems usually have chip sizes on the order of cm^2 and are made of several wafers bonded together, making the mass-production of microfluidic components non-trivial. In addition, the fluidic connection with the external world is also complicated. Moreover, for many applications in biology and chemistry, optical detection methods are used, so optically transparent materials are required in building these microfluidic systems. Therefore, a micro molding replication technique is one possible method to achieve cost effective fabrication, ease of packaging, and optical compatibility. The micro molding replication technique includes mastering and replication processes. In the mastering process, the replication master is fabricated by using high aspect ratio photolithography, electroplating and resist stripping. In the replication process, by using the replication master, microstructures can be transferred to polymer substrates by a hot embossing machine. After obtaining the embossed polymer substrates, they can be bonded to other flat PMMA substrates by a spin-on, UV-cured epoxy resin, or PDMS. Thus, a closed volume microfluidic system can be fabricated. Details of the basic polymer base microfluidic devices fabrication processes developed by our group are discussed in [7].

A micropump is one of the most important devices in microfluidic systems. Various micropump designs have been proposed recently. For those employing mechanical check valves for flow rectification [8], these small and fragile silicon parts are critical problems to overcome, and complicated fabrication processes are involved. Hence, “valve-less pumps” became attractive due to their extremely simple structures. For these pumps, flow rectification is achieved using special channels to generate different flow resistances [9]. From the view point of miniaturization and integration of complex microfluidic systems, simple structures would be valuable in making the entire system more simple and compact. In this paper, a novel valve-less micropump based on vortex flow generation is discussed. Due to its planar and simple structure, the micro molding replication technique is suitable for fabricating such kind of micropump. From our experimental results, the pump rate of our vortex micropump can reach 9.5ml/min at a low operating voltage of 2.5V with power consumption of 165mW. The design, fabrication processes, experimental and simulation results are described in the following sections. We shall show that micro vortex pumping is a new and practical concept for fluidic pumping in a micro-scale environment. Moreover, a fully automated microfluidic platform integrated with a phase-sensitive SPR biosensor is also presented. The system consists of three vortex micropumps and a SPR biosensor head. The entire microfluidic system is fabricated using a low-cost micro molding replication technique. The micropumps are software-controlled to pump different solutions sequentially into the SPR biosensor head. This experimental setup, which has real-time phase extraction and software control capabilities, is used to perform experiments including monitoring of the bovine serum albumin (BSA) binding reaction with BSA antibodies, and cell adhesion properties under the influence of trypsin.

II. DESIGN AND FABRICATION OF VORTEX MICROPUMP

2.1. Design

The vortex micropump uses kinetic energy to move fluid using an impeller and a circular pump chamber. The fundamental design concept is illustrated in Figure 1. The fluid enters the pump near the center of the impeller and is moved toward the outer diameter of the pump chamber by the rotating motion of the impeller. Because of the boundary of the pump chamber, the fluid is guided to enter the microchannel creating the pumping flow. Since the generation of the pumping flow is due to the rotating motion of the impeller, by changing the rotational speed of the impeller, the pumping flow rate can be controlled smoothly.

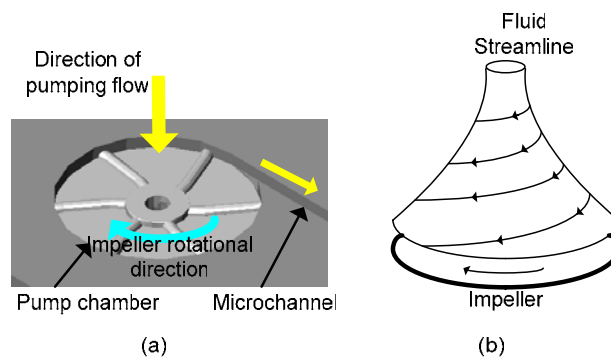


Figure 1. (a) Illustration of the vortex micropump working principle. (b) A fluid streamline inside the pump chamber.

As mentioned earlier, microfluidic devices are required to be optically transparent and bio-compatible for bio-optical detection and many chemical applications. For our vortex micropump, polymethyl methacrylate (PMMA) is the structural material. The micro impeller is placed inside the pump chamber. When the fluid enters the micropump from the center of impeller, the rotational motion of impeller, driven by a DC motor, induces a fluid pressure gradient and thus creates a continuous flow. In our vortex pump design, two structural layers are needed. The lower layer includes the pump chamber and a microchannel, while the upper layer is a cover layer providing the fluidic connection.

2.2. Micro Molding Replication Technique

The micro molding replication technique is a low cost and flexible microfabrication method for polymer based microfluidic systems. It includes two processes: mastering and replication, as illustrated in Figure 2. In the mastering process, the metal mold is fabricated by using high aspect ratio lithography, electroplating and photoresist stripping. Since the required aspect ratio of the microstructures in the vortex pump is relatively high, we chose MicroChemTM SU-8

photoresist as the mold for electroplating, i.e., the metal is electroplated on the photoresist-patterned substrates. After the SU-8 photoresist is striped, the metal mold is fabricated. In the replication process, the enclosed volume of the microfluidic devices are fabricated by the hot embossing process and bonding process. That is, the microstructures on the metal mold is transferred to the PMMA substrates by the hot embossing process. Then, flat PMMA substrates can be bonded to the embossed PMMA substrates by using spin-on interfacial layers such as UV-epoxy or PDMS to achieve enclosed volume microfluidic devices.

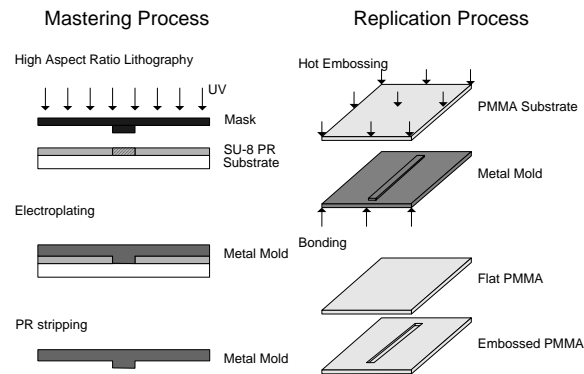


Figure 2. Illustration of the micro mold mastering (left) and replication (right) technique.

2.3. Fabrication of Vortex Micropump

In this section, the fabrication of the micro impeller and the micro mold, replication of the pump chamber and microchannel, and assembly process for the vortex micropump are presented using the aforementioned micro molding replication technique.

2.3.1. Micro impeller batch fabrication process

The fabrication process for the impeller is illustrated in Figure 3. On a Cu coated substrate, MicroChem™ SU-8 2075 photoresist is spun onto the substrate at 3000 rpm. A soft bake is processed at 65°C for 5 minutes and then at 90°C for 20 minutes. Then, SU-8 is exposed under the photoresist mask with the pattern of the impeller circular base. Afterwards, a second layer of SU-8 photoresist is spun onto the first layer at 1500 rpm. Again, it is soft baked and exposed under the photoresist mask with the pattern of the impeller blade, with the proper alignment to the impeller circular base. Another post-expose bake is processed at identical conditions to the first. After this, SU-8 photoresist is developed in SU-8 developer for about 15 minutes at room temperature with mild agitation, it is then rinsed with isopropyl alcohol (IPA) and DI water. The SU-8 impeller is thus fabricated on the substrate. Finally, Cu is etched by the Cu etchant and the stand-alone SU-8 impeller is released from the substrate. The image of SU-8 impeller is shown in Figure 3. The diameters of the

impellers are 2.5mm and 4.5mm. The width of each blade is 150 μ m. The thickness of the circular base and blade is 150 μ m and 250 μ m, respectively.

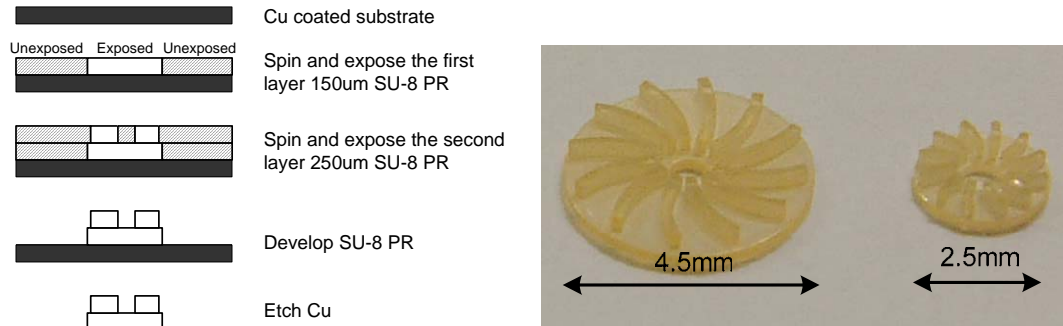


Figure 3. (left) Fabrication process of SU-8 impeller. (right) Photo of SU-8 micro impellers. The diameters of the impellers are 4.5mm and 2.5mm; respectively. The width of each blade is 150 μ m; the thickness of the circular bas is 150 μ m; the thickness of the blade is 250 μ m.

2.3.2. Micro mold of vortex micropump fabrication process

The micro mold functions as a replication master. It includes the pattern of the pump chamber and microchannel. The fabrication process of the micro mold of the vortex micropump is illustrated in Figure 4. On the PMMA substrate, MicroChemTM SU-8 2075 photoresist is spun at 2000 rpm. A soft bake is done at 65 $^{\circ}$ C for 5 minutes then at 90 $^{\circ}$ C for 30 minutes. Then, SU-8 is exposed under the photoresist mask with the pattern of the pump chamber and microchannel. A post-expose bake is processed at 65 $^{\circ}$ C for 5 minutes and then at 90 $^{\circ}$ C for 30 minutes. After that, SU-8 photoresist is developed in SU-8 developer for about 15 minutes at room temperature with mild agitation, and then rinsed with IPA and DI water. After the high aspect ratio lithography process, the 200 μ m thick SU-8 mold of the pump chamber and the microchannel is fabricated. Because of the insulating property of SU-8 photoresist and the PMMA substrate, a 500A Cr adhesive layer and a 3000A Au conductive layer are sputtered on the surface to prepare for the electroplating process. In order to make the micro mold hard and rigid, ultra thick Ni electroplating is necessary. Then, the SU-8 mold is electroplated with Ni using a current density of 40mA/cm² for 15 hours. After removing of SU-8 photoresist and PMMA substrate using MicroChemTM Remover PG, a 1mm thick micro mold of the vortex micropump has been fabricated. In order to easily remove the Ni micro mold from the substrate in the final process, we found that using a PMMA substrate is better than using a silicon substrate. The photo of the micro mold is shown in Figure 4.

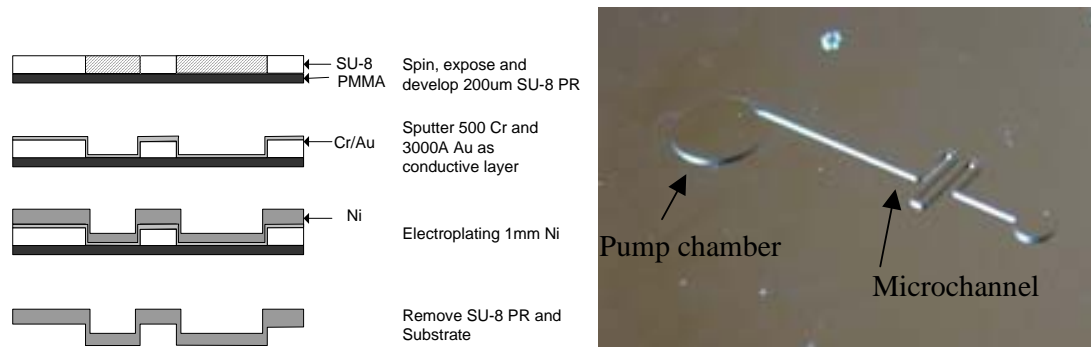


Figure 4. (left) Fabrication process flow for the micro mold of the vortex micropump. (right) Photo of the nickel micro mold of vortex micropump chamber and microchannel.

2.3.3. Vortex micropump replication and assembly process

The micropump replication and assembly processes are shown in Figure 5. In order to replicate the pump chamber and microchannel from the micro mold, the PMMA substrate is heated to 120°C, which is above its glass transition temperature ($T_g = 105^\circ\text{C}$). Then, a pressure of 7MPa is applied by a hydraulic press to compress the micro mold into the PMMA substrate. This causes the microstructures on the micro mold to transfer to the PMMA substrate negatively. After the substrate and the micro mold cools down, the embossed PMMA substrate is released from the micro mold. In order to increase the pump chamber volume, machining tools are used to deepen the chamber. An impeller and a DC motor are assembled on the top and bottom of the chamber, respectively. The inlet and outlet of the micropump is produced by drilling holes through another flat PMMA substrate. Finally, UV-cured epoxy resin is spun on the flat PMMA substrate. The embossed PMMA and the flat PMMA are bonded together to form an enclosed pump chamber with a microchannel between two substrates. A completed vortex micropump with microchannel is shown in Figure 6. The diameter of pump chamber is 5mm. The fluid is pumped through an output microchannel 300µm in width and 200µm in depth.

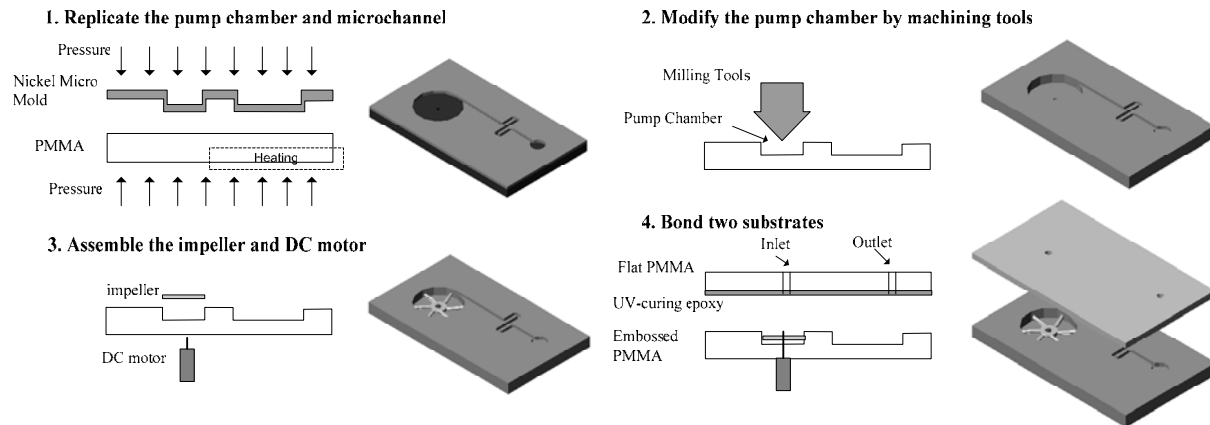


Figure 5. Replication and assembly processes of the vortex micropump.

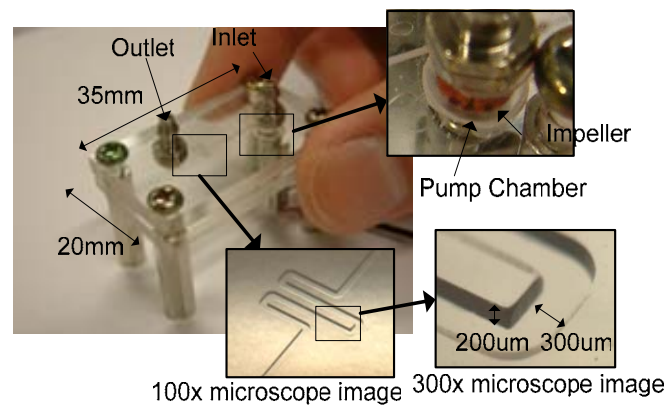


Figure 6. Photo of a vortex micropump with microchannel. The chip size is 20mm × 35mm. The diameter of the pump chamber is 5mm. The output microchannel is 300 μ m in width and 200 μ m in depth.

III. PERFORMANCE OF VORTEX MICROPUMP

The experimental setup for both flow rate and pumping pressure measurements are illustrated in Figure 7. We choose a straight connected microchannel for this experiment, as shown in Figure 8. In both experiments, the far ends of the polyurethane tubes from the micropump are connected to the large open beakers filled with water which act as liquid reservoirs. In the flow rate measurement shown in Figure 7(a), the two beakers are initially set at the same liquid level for equilibrium pressure. The pumping flow rate is approximated from the increased water weight measured by a digital balance over a specific time interval. Because the density of water at STP is 1kg/m³, the flow rate (ml/min) can be directly calculated from the change of water weight (g) over time (min). Because of the large open beakers, the liquid level change

in the beakers during the pumping process is basically constant and the measured flow rate is assumed to be under zero back pressure. In the pumping pressure measurement shown in Figure 7(b), the setup is similar to the one for measuring the volumetric flow rate except that the outlet polyurethane tube is positioned vertically. The liquid level of the outlet polyurethane tube at equilibrium is recorded before the pump is turned on. The pumping pressure is measured from the liquid level change in the outlet polyurethane tube when the maximum height is reached. The measured maximum pumping pressure is assumed to correspond to a zero flow rate.

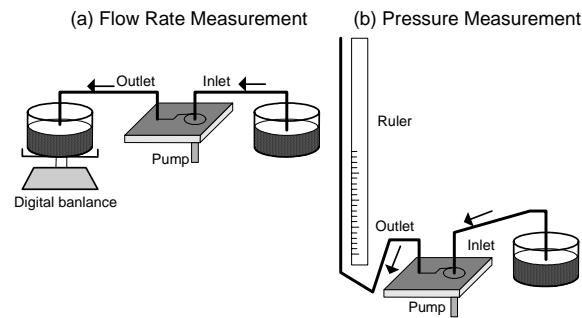


Figure 7. Schematic drawing of the experimental setup. (a) Flow rate measurement under zero back pressure conditions. (b) Pumping pressure measurement under zero flow rate conditions.

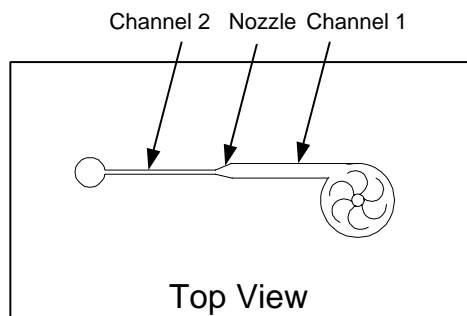


Figure 8. A schematic of the vortex micropump and microchannel configuration used for measurement and analysis.

The pump rate and pumping pressure as a function of the applied voltage are shown in Figure 9(a) and Figure 9(b), respectively. In these figures, we also compare the pump performance of two different size pump chambers, which are 3mm and 5mm in diameter. The output microchannels of all pumps are the same. In general, due to the operating principle of the vortex micropump, the produced fluid flow rate and pressure are directly proportional to the impeller rotational speed. That is, the pump rate and pumping pressure increase linearly with the applied voltage of the DC motor.

Comparing the two different size pump chambers, the difference in pumping performance is evident. A larger pump chamber can produce a higher fluid flow rate and pressure. From the measurement data, the minimum pump rate and pumping pressure are 0.11ml/min and 166Pa at the startup voltage (0.75V) of the DC motor, for the 3mm chamber. The maximum pump rate and pumping pressure are 9.5ml/min and 8000Pa at an applied voltage of 2.5V, for the 5mm chamber.

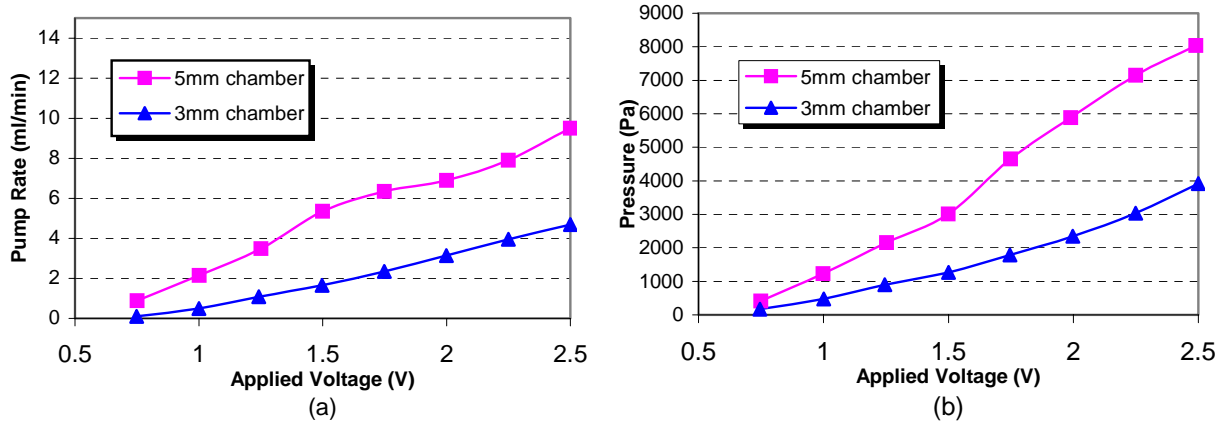


Figure 9. (a) Comparison of pump rate (water is the working fluid) as a function of the applied voltage at zero back pressure. (b) Comparison of pumping pressure (again, water is the working fluid) as a function of the applied voltage at zero flow rate.

IV. MODELING OF VORTEX MICROPUMP

Analytical modeling of the vortex micropump is described in this section. The geometry of the vortex micropump and the connected microchannel is shown in Figure 8. In this section, the theoretical performance of two different diameter pump chambers, 3 and 5mm, respectively, will be compared. The connected microchannel is divided into 3 parts and are referred to as channel 1, nozzle, and channel 2, as shown in Figure 8. Due to the rotation of the impeller, the fluid enters the pump chamber at the center and exits to the microchannel. The fluid pressure is increased by converting the kinetic energy from the impeller. Then, the pressure decreases because of the flow resistance of channel 1, nozzle, and channel 2. Using the physical relationships described in (1), we can formulate an analytical solution relating the pump rate to the impeller rotational speed.

$$P_{produced} = P_{channel1} + P_{nozzle} + P_{channel2} \quad (1)$$

4.1. Pressure increased by the rotation of the impeller

The expression of the pressure produced by the impeller is given in equation (2). The pressure can be calculated from the impeller tip speed, U , and the pump coefficient ψ .

$$P = \psi \rho U^2 \quad (2)$$

In (2), ρ is the density of the fluid. Typical values for the pump coefficient ψ are 0.4 to 0.7 [13]. In our case, two different diameters of pump chamber are compared, i.e., 3 and 5mm. The impeller sizes inside these chambers are 2.5mm and 4.5mm in diameter, respectively. The impeller rotational speed ranges from 8000 to 20,000 rpm. Thus, using the density of water $\rho_{water} = 999 \text{kg/m}^3$, the pump coefficient ψ is estimated experimentally by the least squares method.

4.2. Flow resistance in microchannel

The flow resistance in a microchannel is described by the Hagen-Poiseuille equation [14][15]. For a rectangular microchannel, with a width w , height h , and length l , as illustrated in Figure 10, the flow behavior is assumed to be laminar due to the low Reynolds number, i.e., ~ 74 in our test conditions (estimated using the width of the channel as the characteristic length).

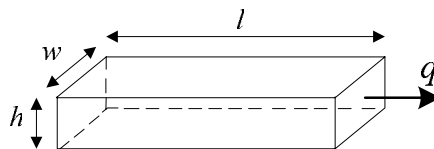


Figure 10. The definition of the rectangular microchannel.

For the rectangular microchannel, the shape factor $\lambda = w/h$ and hydraulic diameter $D_h = 4 \frac{w \cdot h}{2(w+h)}$ can be defined, i.e., the rectangular microchannel is similar to a circular microchannel using a hydraulic diameter analogy. If the shape factor λ is close to one, the volume flow characteristic $\phi(P)$ can be calculated from the Hagen-Poiseuille equation (laminar viscous flow in a constant cross-section channel):

$$\phi(P) = \frac{1}{32} \frac{w \cdot h \cdot P}{\mu \cdot l} D_h^2 \quad (3)$$

where P is pressure difference between the inlet and outlet, and μ is the dynamic viscosity of the fluid. If the shape factor λ is larger than one, the volume flow characteristic $\phi(P)$ is then given by:

$$\phi(P) = \frac{1}{12} \frac{w \cdot h^3}{l} \frac{P}{\mu} \quad (4)$$

In our experiment, the dimensions of channel 1 are $w = 1000\mu\text{m}$, $l = 6000\mu\text{m}$ and $h = 200\mu\text{m}$. And for channel 2 are $w = 300\mu\text{m}$, $l = 12000\mu\text{m}$ and $h = 200\mu\text{m}$. Hence, using $\mu_{\text{water}} = 1.12 \times 10^{-3} \text{ N sec/m}^2$, the shape factor of channel 1 is $\lambda_{\text{channel1}} = 5$, and (4) can be applied to channel 1. And, the shape factor of channel 2 is $\lambda_{\text{channel2}} = 1.5$, (3) can be applied on channel 2. Therefore, the total volume flow characteristic of channel 1 and channel 2 can be calculated from (3) and (4).

4.3. Flow resistance in nozzle

Detailed description of flow in a nozzle can be found in [15]. The two main sources of the pressure drop across a nozzle can be estimated by combining the Hagen-Poiseuille's equations and a modified Bernoulli's equation:

$$P = \frac{128 \cdot \mu \cdot \phi}{3\pi \cdot \tan \alpha} \left(\frac{1}{D_o^3} + \frac{1}{(D_o + l \cdot \tan \alpha)^3} \right) + \frac{8\rho \cdot \phi^2}{\pi^2} \left(x_{sc} \frac{1}{(D_o + l \cdot \tan \alpha)^4} + x_{gc} \frac{1}{\pi D_o^4} + x_{se} \frac{1}{D_o^4} \right) \quad (5)$$

where the first term is the Hagen-Poiseuille equation applied to a duct with D_o as the hydraulic diameter of the inlet of the nozzle (α is the taper angle, l is the length of the nozzle, μ is the dynamic viscosity, ρ is the density of the fluid, P is the pressure difference, and ϕ is the volume flow through the nozzle). The second term is the modified Bernoulli's equation, which is the sum of all additional pressure losses, with x_{sc} as the head loss factor for the sudden contraction at the inlet of the nozzle, x_{gc} as the head loss factor for the gradual contraction due to the pressure drop across the duct, and x_{se} as the head loss factor for the sudden expansion at the outlet of the nozzle.

In our experiment, the dimensions of the nozzle are $Do = 240\mu\text{m}$, $\alpha = 2.6^\circ$, $l = 1000\mu\text{m}$, $\mu_{\text{water}} = 1.12 \times 10^{-3} \text{ N sec/m}^2$ and $\rho_{\text{water}} = 999\text{kg/m}^3$. Since there are no sudden contraction and expansion at the inlet and outlet of the nozzle, $x_{sc} = 0$ and $x_{se} = 0$. For the taper angles of 2.6° , the head loss factor $x_{gc} = 0.02$ [15].

4.4. Comparison of Analytical and Experimental Results

In order to find the mathematical model of the vortex micropump, we can solve the flow rate ϕ as a function of the impeller rotational speed by equation (1) – (5). In Figure 11, the analytical result is plotted in dotted lines, and the experimental result, which is extrapolated from the previous section, is plotted in solid lines. By the least squares method, a pump coefficient of $\psi=0.37$ can be estimated. The in-set of Figure 11 shows the experimental relationship between the rotational speed ω of the impeller motor versus applied DC voltage v . This empirical relationship can be described by a 2nd order polynomial as:

$$\omega = -0.2059 \times 10^4 v^2 + 1.1814 \times 10^4 v + 0.2343 \times 10^4 \quad (6)$$

This expression is used to convert the experimentally applied DC voltages into rotation speeds, which is then used to determine the pump rate versus rotation speed data.

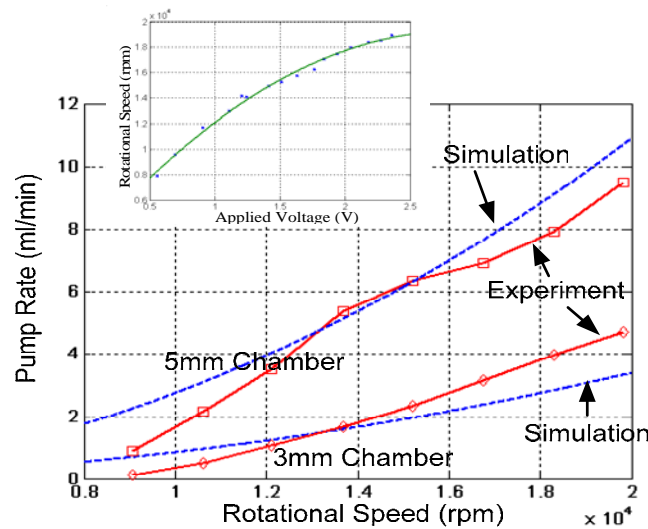


Figure 11. Comparison of the experimental (solid line) and simulation (dotted line) results of pump rate versus impeller rotational speed. The in-set figure shows the experimental relation between rotational speed and applied DC voltage of the impeller motor.

Because of the rudimentary design of our vortex micropump and measurement error, we found that the experimental and analytical results only have a reasonable match. Nevertheless, the analytical results provide an order-of-magnitude estimate to the performance of the vortex pumps. Hence, the analytical equations derived in this work will be useful in helping us to design our future micro vortex pumps.

V. MICROFLUIDIC PLATFORM IN MEDICINE APPLICATIONS

In this section, a fully automated microfluidic platform integrated with a phase-sensitive SPR biosensor is described. The system consists of three vortex micropumps and a SPR biosensor head [16]. The entire microfluidic platform can be fabricated using a low-cost micro molding replication technique. Micropumps are software-controlled to pump different solutions sequentially into the SPR biosensor head. For the SPR sensor, results from our previous work [16] using glycerin-water mixtures indicate that the sensitivity limit of our design can be as high as 5.5×10^{-8} refractive-index units. Such an improvement in the sensitivity limit should put SPR biosensors as a possible replacement of conventional biosensing techniques that are based on fluorescence. We have used our experimental setup, which has real-time phase extraction and software control capabilities, to perform experiments including monitoring of the bovine serum albumin (BSA) binding reaction with BSA antibodies, and cell adhesion properties under the influence of trypsin.

5.1. Surface plasmon resonance sensor

A Kretschmann geometry prism-coupled scheme depicted in Figure 12 is often used in a SPR sensor system. The surface plasmon wave (SPW) vector (k_{sp}) between the metal and dielectric medium can be expressed as:

$$k_{sp} = k_o \sqrt{\frac{\epsilon_{metal} \epsilon_{sample}}{\epsilon_{metal} + \epsilon_{sample}}} \quad (7)$$

where k_o is the free space wave vector of the optical wave, ϵ_{metal} and ϵ_{sample} are the complex dielectric constants of the metal and the sample medium respectively. The enhanced wave vector of incident light (k_i) is given by:

$$k_x = k_o n_{glass} \sin \theta_{inc} \quad (8)$$

where n_{glass} is the refractive index of the prism, and θ_{inc} the angle of incidence. For SPR to take place, which leads to the strongest SPW, the two vectors should be matched. i.e.

$$k_x = k_{sp} \quad (9)$$

The simplest way to express the phase property of SPR is to use the Fresnel equation, the reflection coefficients of the p - and s -polarized light (r_p and r_s), which are given by [17]:

$$r_p = |r_p| e^{i\phi_p} \quad \text{and} \quad r_s = |r_s| e^{i\phi_s} \quad (10)$$

Across the resonant peak, the phase angle will exhibit a steep change, which means that a small variation of ϵ_{sample} or refractive index of sample will lead to a large phase change in the reflected light. Due to the fact that the SPR effect will only affect p -polarized light, the value of phase different ($\Delta\phi$) between p -polarization and s -polarization ($\phi_p - \phi_s$) can be used as a refractive index probe on the sensor surface. (For detailed explanation, see ref [16]).

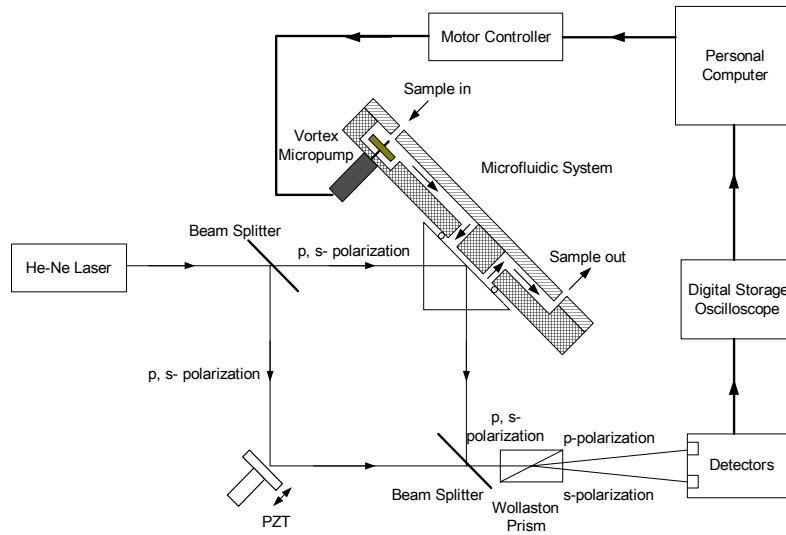


Figure 12. Experimental setup of the microfluidic system integrated with the SPR biosensor.

5.2. Microfluidic platform

The illustration of the automated microfluidic platform is illustrated in Figure 12. Three vortex micropumps and a SPR biosensor are integrated into a polymer-based single chip with a computer to control the flow sequence and to analyse the SPR signals in a real time manner. In this setup, three different solutions can be pumped into the SPR biosensor head independently. A Mach-Zehnder interferometer with a 10mW polarized He-Ne laser operating at 632.8nm is used as the light source. The polarization direction of the output beam is tuned at 30° from *p*-polarization so that a larger amount of light intensity can be contributed to *p*-polarization to enhance the signal-to-noise ratio of the probe beam. For the sensor head, we use a nominally 45nm gold-coated glass plate attached to a 60° equilateral prism made from BASF10 glass using matching oil. The first 50:50 beam splitter divides the laser into two halves. One beam (probe beam) goes to the sensor head while the other beam (reference beam) goes to the plane mirror. A piezoelectric transducer (PZT) is attached to the back of the mirror and a saw-tooth wave oscillating at 120Hz is used to provide the phase modulation signal required by the phase measurement software. Constructive and destructive interference of waves occurred periodically as a time-varying path difference is introduced by the back-and-forth movement of the mirror. The probe beam and reference beam are combined again at the second beam splitter. In the output beam *p*- and *s*-polarization light are separated by the use of Wollaston prism. Two detectors together with a digital oscilloscope are used to capture the signals and finally the differential phase quantity is extracted. Our experimental setup and the microfluidic system are shown in Figure 13.

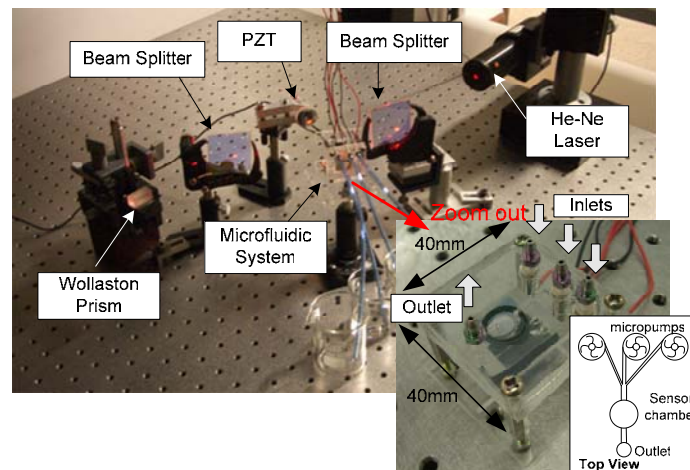


Figure 13. A photo of the polymer-based microfluidic system integrated with a SPR biosensor. The size of the whole chip is 40mm x 40mm. There are three independent inlets for three different solutions.

5.3. Microfluidic platform in medicine applications

5.3.1. Detection of specific binding of biomolecules

In the experiment on biomolecule detection, three types of fluids, namely the buffer, probe and sample fluids were independently introduced into the sensor head. The process sequence is illustrated in Figure 14. The buffer pump first injected a volume of phosphate-buffered saline (PBS) into the sensor head and the differential phase angle was measured as the baseline. A PBS buffer containing BSA (1mg/ml) was then introduced by the probe pump into the sensor head. As shown in Figure 15, the phase angle increased upon the addition of BSA-molecules indicating the binding of BSA onto the gold surface. The system was left to settle for 30mins to allow the formation of a BSA layer on the gold surface. A PBS buffer was then injected by the buffer pump into the sensor head again to wash away the free BSA. Then, a PBS buffer containing non-BSA antibodies (Rat IgG) was injected by the sample pump into the sensor head to test whether there was any nonspecific binding. The differential phase remained constant afterward, thus confirming that no nonspecific binding had taken place. PBS buffer containing BSA specific antibodies was then pumped into the sensor head using the sample pump. A sharp increase in phase angle was observed, indicating the binding reaction of BSA with the BSA antibodies. An exponential curve characteristic to typical rate-dependent reactions was also noticed. Since a concentration of $37\mu\text{g/ml}$ of BSA corresponds to an absolute phase change of 34.4° , we estimate that the detection sensitivity of our setup is 10.76ng/ml (based on 0.01° resolution). Finally, PBS was injected again. The phase angle remained constant, which shows that the sensor surface has been fully saturated by BSA antibodies due to the specific binding reaction and the additional BSA antibodies could not find any space on the sensor surface to bind to.

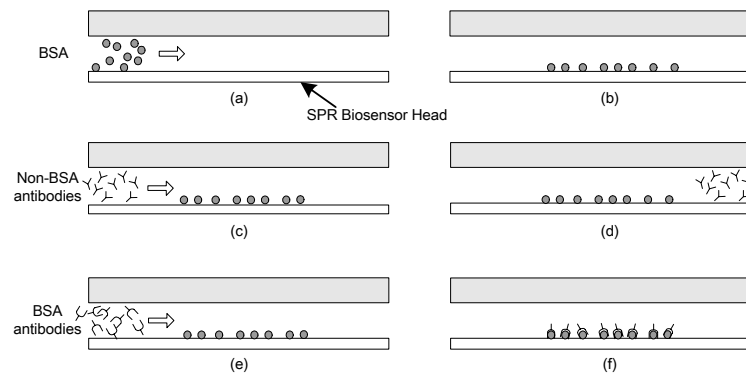


Figure 14. Illustration showing detection of specific antibody binding. (a) Injection of BSA. (b) Forming of a layer of BSA on the sensor head. (c) Injection of nonspecific BSA antibodies (Rat IgG). (d) Removal of non-specific antibodies without any binding. (e) Injection of specific BSA antibodies. (f) Specific binding of BSA to BSA antibodies.

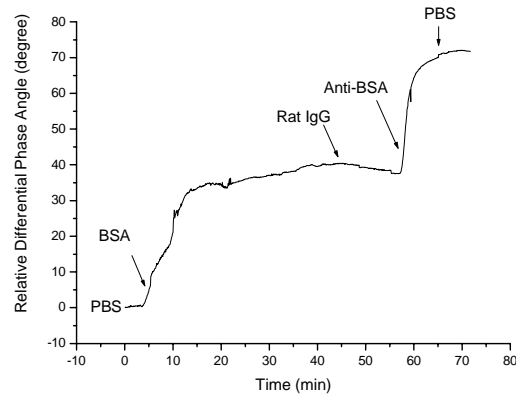


Figure 15. Response curve of differential phase angle after sequential addition of PBS, BSA, nonspecific BSA antibody (Rat IgG), and BSA antibody into the sensor head, demonstrating the detection of specific BSA-anti-BSA binding.

5.3.2. Cell detachment by adding trypsin

A. Material

The cells that we used in our experiment were mouse L929 cell (4×10^6 cells/ml) obtained from ATCC (American Type Culture Collection). Prior to the experiment, the mouse cells were put in a rich nutrient buffer, RPMI Medium 1640 from Invitrogen Corporation. RPMI (Roswell Park Memorial Institute) Medium 1640 is a liquid medium with enriched formulations for culturing living mammalian cells. With the aid of RPMI, living L929 cells will naturally attach to the gold surface. Trypsin-EDTA (0.25% Trypsin) obtained from Invitrogen Corporation is a common reagent used to remove and detach cells from culture substratum. Trypsin was thus used in our experiment to detach the cells from the gold surface by breaking the adhesion proteins between the cell and the gold surface.

B. Results

The process sequence is illustrated in Figure 16. Mouse L929 cells (4×10^6 cells/ml) were first cultured on a 45nm gold-coated glass plate at 37°C for two hours. Then the gold surface was observed under an optical microscope to ensure cells were well adhered to the glass plate. As shown in the in-set of Figure 17, cells were adhered on the gold surface as a monolayer. This glass plate was then attached to a prism using matching oil for phase-sensitive SPR bio-sensing studies. RPMI Medium 1640 was first flowed into the chamber to measure a baseline differential phase. Trypsin-EDTA (0.25% Trypsin) was then injected into the sensor head. As shown in Figure 17, an exponential decay curve was observed indicating that the cells were detached from the gold surface. Finally, RPMI was circulated to ensure all the cells

were suspended. Another set of control experiments were carried out by repeating the experiment with bare gold glass plate. A small phase angle changed was observed when trypsin is added. Thus, we conclude that the large phase change observed in Figure 17 must be largely caused by cell detachment. At the end of the experiment, the glass plate was taken out from the prism and observed again under an optical microscope. Visual inspection confirmed that almost all the cells were removed from the surface. Our results show that one can monitor cell detachment affinities using SPR. This is a very useful platform for a range of bio-medical applications e.g. drug discovery by simply replacing trypsin with newly invented drugs.

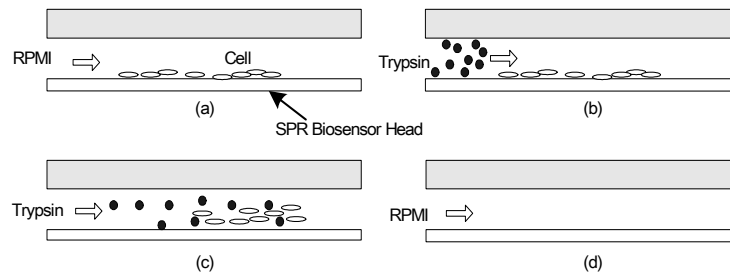


Figure 16. Illustration of cell detachment detection mechanism. (a) Injection of RPMI. (b) Injection of trypsin. (c) Detaching cell from the sensor head. (d) No cell left on the sensor surface

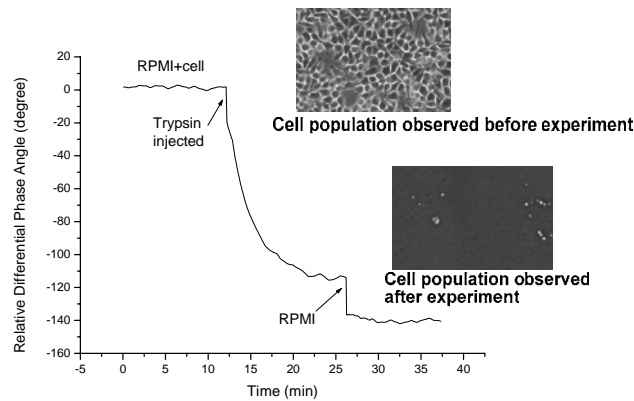


Figure 17. Differential phase response curve due to sequential addition of RPMI containing cells, trypsin, and RPMI into the sensor head.

VI. CONCLUSION

In this paper, a novel polymer based vortex micropump is presented. Detailed fabrication processes, performance characteristics and analytical modeling of the vortex micropump are provided. For a pump chamber of 5mm, the maximum measured pump rate is 9.5ml/min at a low operating voltage of 2.5V. An advantage of the vortex micropump is that the pump rate and pumping pressure increase linearly with the applied voltage of a DC motor. Combining fluid transmission, fluid multiplexing, fluid mixing, temperature control, and digital pumping control into a single fluidic chip; less bulky and low-cost systems can be developed based on our micro vortex pumps. Detection of bio-specific protein partners (BSA and BSA-antibody) and monitoring of cell adhesion activities have been successfully demonstrated using our new SPR biosensor integrated with the automated microfluidic system. This preliminary study on cell activity showed the possibilities of using differential phase SPR bio-sensors in a wide range of bio-medical applications. Our integrated system should provide a useful platform for conducting high-throughput diagnostic tests on cells and biomolecules at a very low cost. Furthermore, arrayed sensing surface with multiple analytes and parallel detection by using a 2-D phase imaging technique will certainly be a very exciting direction for further development of phase-sensitive SPR sensors.

REFERENCES

- [1] M. Kohl, D. Dittmann, E. Quandt and B. Winzek, "Thin film shape memory microvalves with adjustable operation temperature", *Sensors and Actuators*, vol. 83, pp. 214-219, 2000.
- [2] S. Li and S. Chen, "Analytical analysis of a circular PZT actuator for valveless micropumps", *Sensors and Actuators*, vol. 104, pp. 151-161, 2003.
- [3] Z. Yang, M. Matsumoto and H. Goto and R. Maeda, "Ultrasonic micromixer for microfluidic systems", *Sensors and Actuators*, vol. 93, pp. 266-272, 2001.
- [4] D. Baechi, R. Buser and J. Dual, "A high density microchannel network with integrated valves and photodiodes", *Sensors and Actuators*, vol. 95, pp. 77-83, 2002.
- [5] G. Bedo, H. Fannasch and R. Muller, "A silicon flow sensor for gases and liquids using AC measurements", *Sensors and Actuators*, vol. 85, pp. 124-132, 2000.
- [6] T. Thorsen, S. J. Maerkl and S. R. Quake, "Microfluidic large-scale integration", *Science*, vol. 298, pp. 580-584, 2002.
- [7] Winnie W. Y. Chow, Kin Fong Lei, Guanyi Shi, Wen J. Li and Qiang Huang, "Low Temperature Polymer-Based Substrates Bonding Using PDMS for Micro Fluidic Applications", *Asia-Pacific Conference of Transducers and Micro-Nano Technology (APCOT MNT 2004)*, July, Japan, 2004.

- [8] R. Linnemann, P. Woias, C. D. Senfft and J. A. Ditterich, "A self-priming and bubble-tolerant piezoelectric silicon micropump for liquids and gases", *IEEE MEMS 1998*, pp. 532-537, 1998.
- [9] A. Olsson, O. Larsson, J. Holm, L. Lundblad, O. Ohman and G. Stemme, "Valve-less diffuser micropumps fabricated using thermoplastic replication", *IEEE MEMS 1997*, pp. 305-310, 1997.
- [10] K. S. Yun, I. J. Cho, J. U. Bu, C. J. Kim and E. Yoon, "A surface-tension driven micropump for low-voltage and low-power operations", *Journal of Microelectromechanical Systems*, vol. 11, no. 5, pp. 454-461, 2002.
- [11] S. Bohm, W. Olthuis and P. Bergveld, "A plastic micropump constructed with conventional techniques and materials", *Sensors and Actuators*, vol. 77, pp. 223-228, 1999.
- [12] J. H. Tsai and L. Lin, "A thermal-bubble-actuated micronozzle-diffuser pump", *Journal of Microelectromechanical Systems*, vol. 11, no. 6, pp. 665-671, 2002.
- [13] J. Tuzson, *Centrifugal pump design*, Wiley, 2000.
- [14] S. Bendib and O. Francais, "Analytical Study of Microchannel and Passive Microvalve, Application to Micropump Simulator", *Design, Characterization and Packaging for MEMS and Microelectronics II, Proceedings of SPIE*, 17-19 December 2001, Adelaide, Australia, 2001.
- [15] M. Koch, A. Evans, A. Brunnschweiler, *Microfluidic Technology and Applications*, pp.3-16, Research Studies Press Ltd., 2000.
- [16] S. Y. Wu, H. P. Ho, W. C. Law, C. Lin and S. K. Kong, "Highly Sensitive Differential Phase-sensitive Surface Plasmon Resonance Biosensor Based on the Mach-Zehnder Configuration", *Optics Letters*, vol. 29, no. 20, pp.2378-2380, March 2004.
- [17] P. Yeh, *Optical Waves in Layered Media*, Wiley, New York, 1988.